nucGEMs probe the biophysical properties of the nucleoplasm

Tamás Szórádi[1*], Tong Shu[1*], Gururaj R. Kidiyoor[1*], Ying Xie[1], Nora L. Herzog[1], Andrew Bazley[1], Martina Bonucci[1], Sarah Keegan[1], Shivanjali Saxena[1], Farida Ettefa[1], Gregory Brittingham[1], Joël Lemiere[2], David Fenyö[1], Fred Chang[2], Morgan Delarue[3], and Liam J. Holt[1].

[1]Institute for Systems Genetics, New York University School of Medicine, New York, NY, USA, [2]Department of Cell and Tissue Biology, University of California San Francisco, San Francisco, CA, USA, [3]Laboratoire d'analyse et d'architecture des systèmes, Toulouse, France.

* These authors contributed equally to this work

Correspondence: liam.holt@nyulangone.org

Abstract

The cell interior is highly crowded and far from thermodynamic equilibrium. This environment can dramatically impact molecular motion and assembly, and therefore influence subcellular organization and biochemical reaction rates. These effects depend strongly on length-scale, with the least information available at the important mesoscale (10-100 nanometers), which corresponds to the size of crucial regulatory molecules such as RNA polymerase II. It has been challenging to study the mesoscale physical properties of the nucleoplasm because previous methods were labor-intensive and perturbative. Here, we report nuclear Genetically Encoded Multimeric nanoparticles (nucGEMs). Introduction of a single gene leads to continuous production and assembly of protein-based bright fluorescent nanoparticles of 40 nm diameter. We implemented nucGEMs in budding and fission yeasts and in mammalian cell lines. We found that the nucleus is more crowded than the cytosol at the mesoscale, that mitotic chromosome condensation ejects nucGEMs from the nucleus, and that nucGEMs are excluded from heterochromatin and the nucleolus. nucGEMs enable hundreds of nuclear rheology experiments per hour, and allow evolutionary comparison of the physical properties of the cytosol and nucleoplasm.

Main

The cell interior is a highly complex crowded environment that contains polymer meshes and dense colloidal solutes of a wide range of sizes(Kate Luby-Phelps 2013; Zidovska 2020). Molecular motors and dynamic polymers create an active system that is far from equilibrium. This environment strongly influences biological reactions. One example of how the cell interior impacts biochemistry is through molecular crowding effects(Zhou, Rivas, and Minton 2008). High concentrations of crowding agents entropically favor intermolecular associations, thereby accelerating reaction rates(Rivas and Minton 2018). On the other hand, excessive crowding can also dramatically decrease molecular motion. Active processes are thought to increase the effective temperature in the cell, helping to fluidize this extreme environment. Indeed, depletion of ATP can lead to glass transitions(Parry et al. 2014). However, these glassy transitions strongly depend on length-scale: molecules with sizes equivalent to or larger than the dominant crowding agent will be more affected than small particles that can move through the gaps between larger jammed particles. For instance, in the absence of ATP, the bacterial cytosol is liquid at the nanometer length-scale of individual proteins, but becomes glassy for particles at the mesoscale (tens to hundreds of nanometers)(Parry et al. 2014). Crowding was recently demonstrated to be actively regulated at the mesoscale in the cytosol due to changes in ribosome concentration, and these changes in crowding can tune large-scale molecular assembly by phase separation(Delarue et al. 2018). However, there is still limited information about mesoscale molecular crowding in other organelles, including the nucleus.

Physical characterization within the nucleus of a living cell is challenging. Tracking of synthetic chromosomal loci(Marshall et al. 1997)(Heun et al. 2001), beads larger than 100 nm(de Vries et al. 2007; Tseng et al. 2004)(Hameed, Rao, and Shivashankar 2012), and inhomogeneities in chromatin staining(Zidovska, Weitz, and Mitchison 2013) have provided rich information about the dynamics of chromatin, but there is limited information about the properties of the fluid phase of the nucleus, the nucleoplasm. One technique that can provide extensive information about soft condensed matter is microrheology, which infers the properties of

materials from the motion of tracer particles. These probes should be as passive as possible to avoid difficulties in interpretation due to binding to structures within the cell. Previous approaches to microrheology relied on the introduction of non-biological probes by microinjection(K. Luby-Phelps, Taylor, and Lanni 1986; Crick, FHC and Hughes, AFW 1950) or pinocytosis(Etoc et al. 2018), but these approaches are prohibitively labor intensive, and impossible for organisms with a cell wall, (e.g. fungi, bacteria). Fluorescence recovery after photobleaching (FRAP) and fluorescence correlation spectroscopy (FCS) experiments have provided valuable information about the nanoscale properties of the nucleoplasm(Phair and Misteli 2000), but individual fluorescent proteins are too small (~ 3 nm in diameter) to report on the mesoscale environment.

To overcome this limitation, we recently developed genetically encoded nanoparticles based on naturally occurring homomultimeric scaffold proteins fused to fluorescent proteins(Delarue et al. 2018). In particular, we have focused on encapsulins as scaffolds, which assemble into particles of 40 nm diameter in the cytosol. We called these mesoscale probes Genetically Encoded Multimeric nanoparticles, or GEMs. GEMs allow us to probe both local and global biophysical properties of the cell in high throughput. Here, we extended this technology to the study of the rheological properties of the nucleoplasm. By introducing a nuclear localization signal (NLS) on the encapsulin protein, we directed GEMs to assemble within the nucleus. We refer to these new probes as nucGEMs, and to disambiguate, in this report we will refer to the previously reported cytosolically localized particles as cytGEMs.

Results

Nanoparticle design

A schematic of the nucGEM described is shown in Fig. 1a. Our original GEM design was maintained; we used an encapsulin from *Pyrococcus furiosus* as our scaffold protein, and fused the T-Sapphire (T203I) variant of GFP(Zapata-Hommer and Griesbeck 2003; Ehrig, O'Kane, and Prendergast 1995) to the C-terminus (Delarue et al. 2018). Additionally, we included the A206K mutation that prevents dimerization of the fluorophore (thus, mT-Sapphire)(von Stetten et al. 2012). The encapsulin scaffold drives multimerization of the monomer into a T = 3 icosahedral structure(Akita et al. 2007). The topology of this domain places the N-terminus within the lumen of the assembled particle and the C-terminus on the outside, thus a dense cloud of mT-Sapphire fluorophores faces the cellular environment. We empirically determined that mT-Sapphire gave the brightest particles when imaged using a standard 488 nm laser illumination and emission filters designed for GFP (bandpass from 508 to 544 nm, ET525/36m, Chroma). Importantly, we determined that the optimal excitation of mT-Sapphire was shifted such that it was best excited by 488 nm light in the context of GEMs, presumably due to altered photochemistry on the crowded surface of the nanoparticles. We also found that mT-Sapphire photoactivated in the context of GEMs, which is convenient as particle intensity actually increases during the first few seconds of imaging. We modified the design of cytosolic GEMs by adding a nuclear localization signal (NLS) from SV40. We initially explored gene designs in the budding yeast *Saccharomyces cerevisiae*. We tried appending the NLS to either the C-terminus or N-terminus of the encapsulin monomer. We found that both designs resulted in localization of nucGEMs within the nucleus (Fig 1b; Supplementary Fig. 1a); however the C-terminal NLS appeared to lead to occasional strong interactions with the nuclear periphery, as revealed in time projections showing long residence times at the edges of the nucleus (Supplementary Fig. 1a), lower overall effective diffusion (Supplementary Fig. 1b), and stronger ergodicity breaking than N-terminally tagged nucGEMs (Supplementary Fig. 1c, see below and methods for further explanation). These strong interactions are probably due to high valency interactions of the multiple NLS peptides on the particle surface with the nuclear transport machinery. The N-terminal NLS signal on the other hand is ultimately buried inside the particle and therefore inaccessible to the nuclear transport machinery. Therefore, the monomer or subassemblies must be imported through the nuclear pore prior to assembly of nanoparticles within the nucleoplasm (Fig. 1a). As a result, the surface of nucGEMs is precisely the same as cytGEMs. Therefore, differences in interactions with the cell are not a concern. Fig. 1b compares the localization and tracks from cytGEMs and nucGEMs. Comparison with the

localization of an mCherry-tagged Nup49 nuclear pore marker shows that nucGEMs are confined within the nucleus (Fig. 1b, right). Therefore, we settled on the N-terminal NLS as our design for nucGEMs and now have a genetically encoded tool to study the mesoscale microrheology of the nucleoplasm.

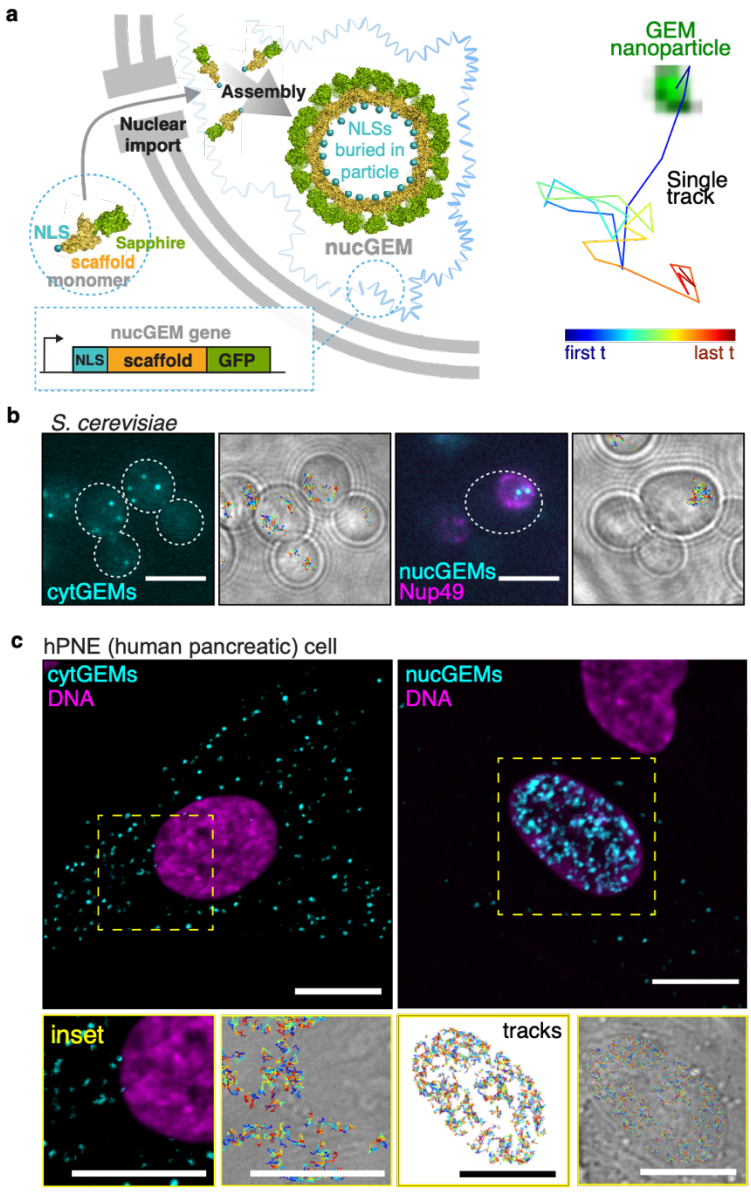

Fig. 1: Genetically encoded nanoparticles can be targeted to assemble in the nucleus.
a, Schematic of nucGEMs. The nucGEM gene, integrated into the genome, encodes an N-terminal nuclear localization signal on a *Pyrococcus furiosus* encapsulin scaffold, and a C-terminal mT-Sapphire fluorophore. The nucGEM monomer is imported into the nucleus, and then assembles to form a 40 nm diameter nanoparticle. **b**, Representative images of cytosolic cytGEMs (cyan, left) and nuclear nucGEMs (cyan, right, with Nup49-ymRuby in magenta marking the nuclear envelope) in *Saccharomyces cerevisiae*. Also shown, tracks from movies (Supplementary Video 1) projected onto brightfield images. Scale bar represents 5 μm. **c**, Representative images of cytosolic cytGEMs (cyan, left) and nuclear nucGEMs (right) in human pancreatic nestin expressing (hPNE) cells. SiR-DNA dye indicates the position of the nucleus in both images. Insets show tracks from movies (Supplementary Video 2). Scale bar represents 10 μm.

nucGEMs in fission yeast and mammalian cells

Cytosolic GEMs have been a powerful tool to compare the mesoscale physical properties of different organisms(McLaughlin et al. 2019; Delarue et al. 2018; Molines et al. 2020). Therefore, we next sought to implement nucGEMs in the fission yeast *Schizosaccharomyces pombe* and in mammalian cells. By comparison to the localization of an mCherry tagged Ish1 nuclear envelope marker *(REF)*, we found that 40nm-nucGEMs were also located within the nucleus of *S. pombe* (Supplementary Fig. 2). Next, we introduced 40nm-GEMs into two human cell lines, a karyotypically normal immortalized human pancreatic nestin-expressing cell line (hPNE)(K. M. Lee et al. 2003)(Fig. 1c) and the widely used HeLa epidermoid carcinoma cell line(Scherer, Syverton, and Gey 1953)(Supplementary Fig 3a). We compared the growth-rate of HeLa cells to cells stably transfected with nucGEMs and found no significant difference, indicating that the presence of these nanoparticles is not toxic (Supplementary Fig 4a). We also assessed the overall metabolic rate using PrestoBlue Cell Viability reagent and found no significant difference between control HeLa cells and nucGEM expressing HeLa cells (Supplementary Fig 4b). Previous studies found that cytGEMs are well tolerated(Carlini et al. 2020); these results indicate that nucGEMs also do not greatly perturb cell physiology.

Using the vital stain SiR-DNA (a far-red derivative of Hoechst dye, Spirochrome) we found that nucGEMs were in the nucleus of both mammalian cell lines (Fig. 1c; Supplementary Fig. 3a). However, there were also particles in the cytosol. nucGEMs are far too large to pass through nuclear pores, which have a passive diffusion size limit of around 5 nm(Mohr et al. 2009). Therefore, we hypothesized that nucGEMs might be released from the nucleus when the nuclear envelope breaks down during mitosis. This would not occur in *S. cerevisiae* because the nuclear envelope remains intact during the closed mitosis of this organism(Boettcher and Barral 2013). We occasionally found nucGEMs in the cytoplasm of *S. pombe*, which could be due to the occasional assembly of particles prior to import, or possibly due to leakage from holes in the nuclear envelope that can appear at the spindle pole bodies during anaphase(Dey et al. 2020). Also consistent with the mitotic ejection hypothesis, we observed that all nucGEMs were confined to the nucleus in post-mitotic murine neurons (Supplementary Fig. 3b).

We next performed time-lapse imaging to directly address the hypothesis that nucGEMs are ejected from the nucleus during mammalian mitosis (Fig. 2). To visualize the localization of nucGEMs throughout mitosis, hPNE cells expressing nucGEM cells were synchronized in G2 with the reversible CDK1 inhibitor r3306. We imaged z-stacks of cells expressing nucGEMs motion every 15 minutes during cell division (Supplementary Video 3). Still images from a representative cell are shown in Fig. 2a. In late G2, the majority of nucGEMs are nuclear, as quantified by the average total fluorescence intensity of GEMs in the nucleus and cytosol in Fig 2b (n = 7). Upon chromosome condensation during prophase, nucGEMs became excluded from chromatin and were released into the cytosol upon dissolution of the nuclear envelope. This chromatin exclusion continued through cell division, and upon nuclear reassembly at telophase, very few GEMs remained in the daughter nuclei and were instead mostly in the cytosol. Subsequently, new nucGEMs slowly assembled and accumulated in the nucleus, while the concentration of nucGEMs in the cytosol slowly decreased, perhaps due to degradation and autophagy (Fig. 2c). Together, these observations support the hypothesis that nucGEMs assemble in the nucleus, are too large to passively diffuse through nuclear pores, and are ejected from the nucleus during mitosis in dividing cells. We later found the resulting presence of GEMs in both the nucleus and cytosol to be very useful in comparing the properties of these compartments in the same cell, as discussed below.

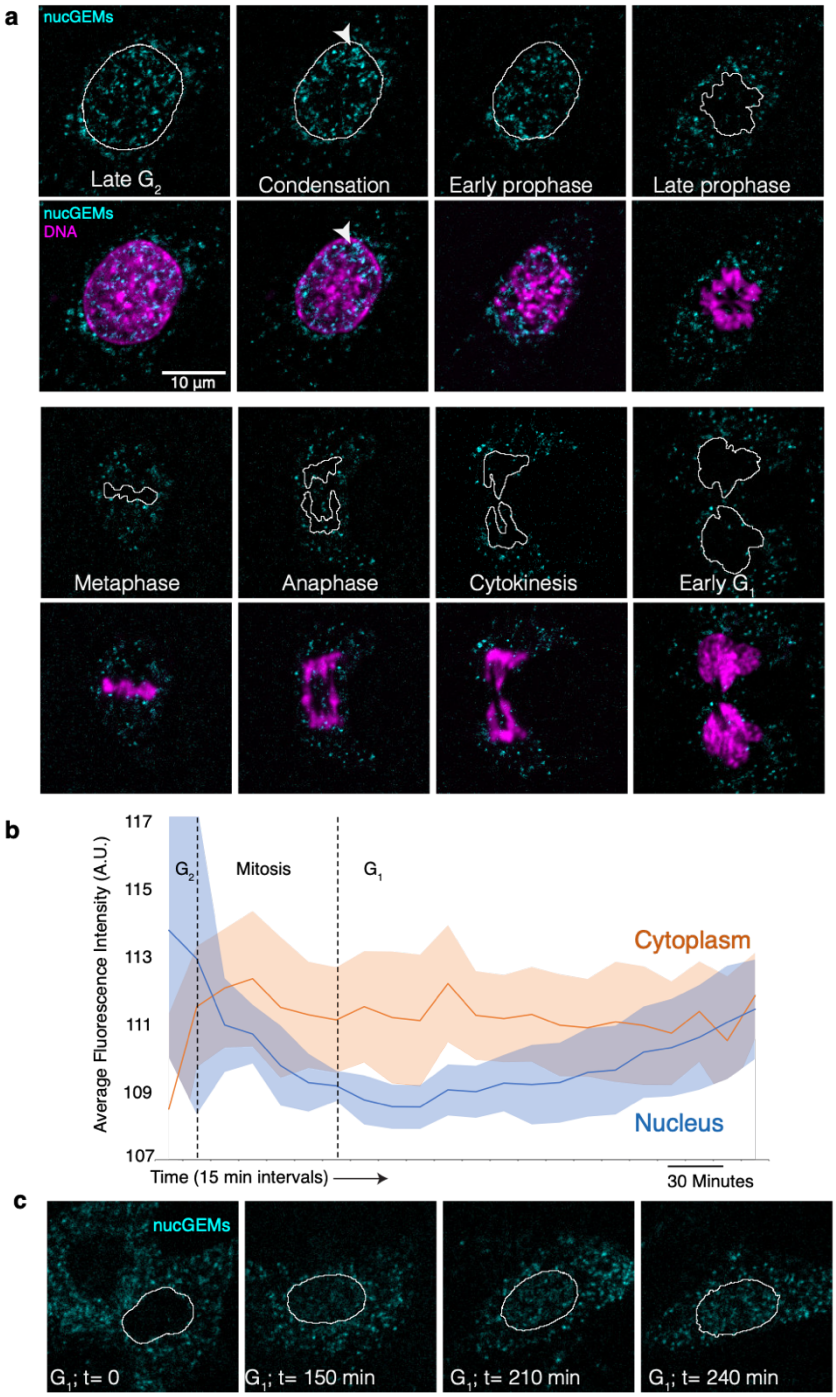

Fig. 2: Mammalian nucGEMs assemble in the nucleus in interphase and are ejected during mitosis. a. Representative confocal micrographs of an hPNE cell expressing nucGEMs undergoing mitosis. nucGEMs are shown in cyan and DNA in magenta. **b.** Average fluorescence intensity of nucGEMs showing the loss and recovery of nucGEMs from the nucleus during and after mitosis. Lines represent median intensity, shaded area indicates standard deviation, n = 7. **c**, Representative confocal micrographs of an hPNE cell accumulating nucGEMs in the nucleus during the first four hours post-mitosis.

nucGEMs are excluded from nucleoli and preferentially explore euchromatin

The expulsion of nucGEMs from mitotic chromatin is consistent with previous work that showed that ribosomes and cytGEMs are excluded from condensed chromosomes by a mechanism involving Ki-67(Cuylen-Haering et al. 2020). This suggests that condensed chromatin could be extremely effective at excluding mesoscale particles of > 25 nm diameter (the diameter of ribosomes). However, nucGEMs do assemble and move within the interphase nucleus (Fig. 1). We additionally noticed that nucGEM tracks were mainly observed in regions of the nucleus with faint SiR-DNA straining, and appeared to be excluded from both brightly stained regions and large unstained regions. SiR-DNA binds preferentially to A/T-rich DNA, and brighter staining is thought to correspond to dense heterochromatin. On the other hand, nucleoli are typically very poorly stained by SiR-DNA and appear as dark patches. Therefore, we hypothesized that nucGEMs were excluded from heterochromatin and nucleoli. First, we compared nucGEM time projections to the Nop4 nucleolar protein N-terminally tagged with mCherry in *S. cerevisiae* and found complete exclusion from the nucleolus in this organism (Fig. 3a). Next, we used immunofluorescence staining to visualize the NPM1 nucleolar marker in hPNE and HeLa cells (Fig 3b; Supplementary Fig. 3a) and again found exclusion from nucleoli. We also looked at sc35 marker for nuclear speckles, which are also thought to be condensates(Fu and Maniatis 1990). Again, nucGEMs were excluded from nuclear speckles (Supplementary Fig. 3b). Finally, we visualized heterochromatin using antibodies against histone H3 tri-methyl lysine 9 marks (H3K9me3), and euchromatin using histone H3 acetyl-lysine 27 marks (H3K27ac) and found slight anticorrelation with the former and correlation with the latter (median Pearson R -0.027 and +0.2316 respectively), indicating that nucGEMs are relatively excluded from heterochromatin and tend to be found mostly within euchromatic DNA (Fig. 3c). Together, these results suggest that densely packed heterochromatin and phase-separated nucleoli in interphase cells have low permeability to mesoscale particles of 40 nm diameter.

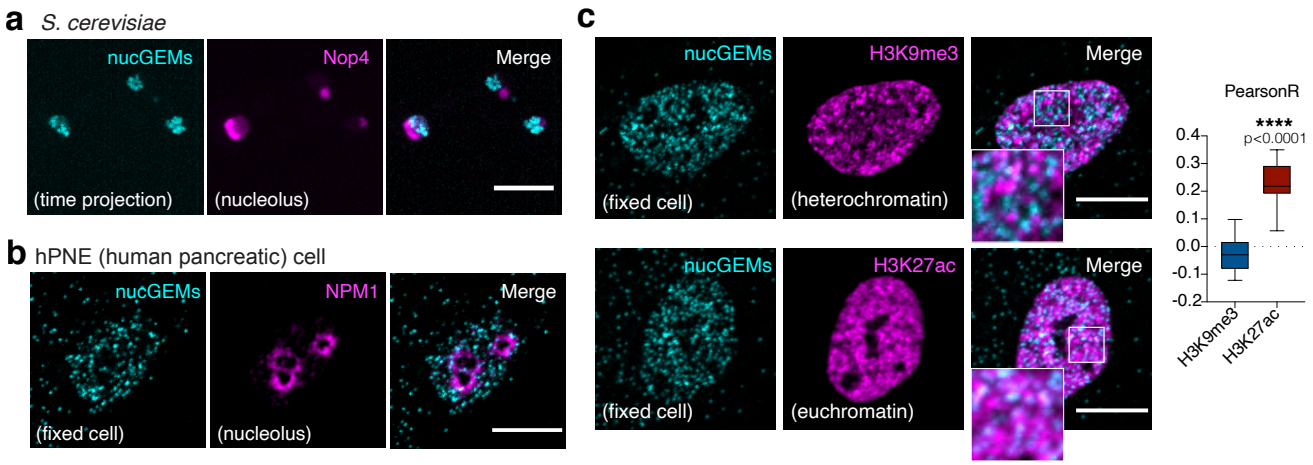

Fig. 3: nucGEMs are excluded from nucleoli and heterochromatin. a. Representative images of nucGEMs (Cyan) from time-projection of the 4 sec movie, Nop4 tagged with mCherry indicates the nucleolus (magenta), scale bar represents 5 μm. **b.** Representative confocal image of hPNE cell expressing nucGEMs (Cyan) stained with nucleolar marker nucleophosmin 1 (in magenta). Scale bar represents 10 μm **c. (left)** Representative confocal micrographs of an hPNE cell expressing nucGEMs stained with heterochromatic marker H3K9 tri-methylation or with active or euchromatin marker H3K27 acetylation (in magenta). Scale bar represents 10 μm. **(right)** box plot of Pearson correlation coefficients of image pixel intensities for nucGEMS and H3K9me3 (n=18) or H3K27ac (n=17); Boxplot-whiskers represent min and max value; p-value from a Student's t-test (**** p< 0.0001).

nucGEMs probe the mesoscale properties of the nucleoplasm

The nucleus has been reported to maintain a lower mass density than the cytosol by volume scaling throughout the cell cycle, while the nucleolus has the highest mass density of any compartment(Kim and Guck 2020). In addition, the nucleus has been reported to be less crowded than the cytosol at the nanometer length-scale of single GFP molecules(Phair and Misteli 2000). However, there is very little information regarding the mesoscale properties of the nucleoplasm. We therefore collected large datasets to compare the rheological properties of the nucleoplasm and cytosol in *S. cerevisiae*, *S. pombe*, and the hPNE and HeLa mammalian cell lines. We imaged nucGEMs and cytGEMs at 100 Hz (100 frames per second) using a spinning-disk confocal for mammalian cells and Highly inclined thin illumination (HILO TIRF)(Tokunaga, Imamoto, and Sakata-Sogawa 2008) for *S. cerevisiae* and *S. pombe*. We limited our analysis to particles that were tracked for longer than 10 time points and curtailed all mean-squared trajectories to this same 100 ms timescale when comparing individual tracks. Analysis of the mean square displacement (<MSD>) produced by time-averaging of these particle trajectories at a timescale of 100 ms allowed for determination of the effective diffusion coefficient (D_{eff}) of each particle(Delarue et al. 2018). For all organisms, there is significant variation in the mobility of individual particles in both the nucleus and the cytosol (Figs. 4a, d; Supplementary Figs. 8a and 9a). In contrast to previous results at the nanoscale in mammalian cells(Phair and Misteli 2000), both individual trajectory analysis and ensemble-time averaging analysis show that, at the mesoscale in *S. cerevisiae* and mammalian cells, median nucGEM mobility measured at the 100 ms time-scale is lower in the nucleus compared to the cytGEMs in the cytosol (Fig. 4a, 4c, 4d and 4e). This lower mobility could indicate more frequent collisions with crowders or cellular structures (such as chromatin) within the nucleus at the 40 nm length-scale. Comparison of median α values from individual trajectories at the same 100 ms time-scale (α_{100ms}) showed no significant difference between the anomalous exponent in the nucleus and cytosol (Fig. 4a). However, for *S. cerevisiae* (Fig. 4b) and human cell lines (hPNE, Fig. 4e, and HeLa, Supplementary Fig. 9b), ensemble-time averaging analysis for all trajectories with length greater than 10 (α_{100ms}), gave a lower α_{100ms} in the nucleus. One interpretation for this lower α_{100ms} could be a higher level of confinement in the nucleus. This difference remains consistent over an order of magnitude of time-scales when analyzing minimum trajectory lengths of 20, 50, or 100 for *S. cerevisiae* (Supplementary Fig. 7a).

In contrast to *S. cerevisiae* and mammalian cell lines, the D_{eff} of the *S. pombe* nucleus was higher than that of the cytosol (Supplementary Fig. 8a, c), although the nucleus still displayed a smaller α_{100ms} than the cytosol (Supplementary Fig. 8b). It will be interesting to see how these differences in nuclear rheology may reflect differences in nucleoplasmic composition and architecture.

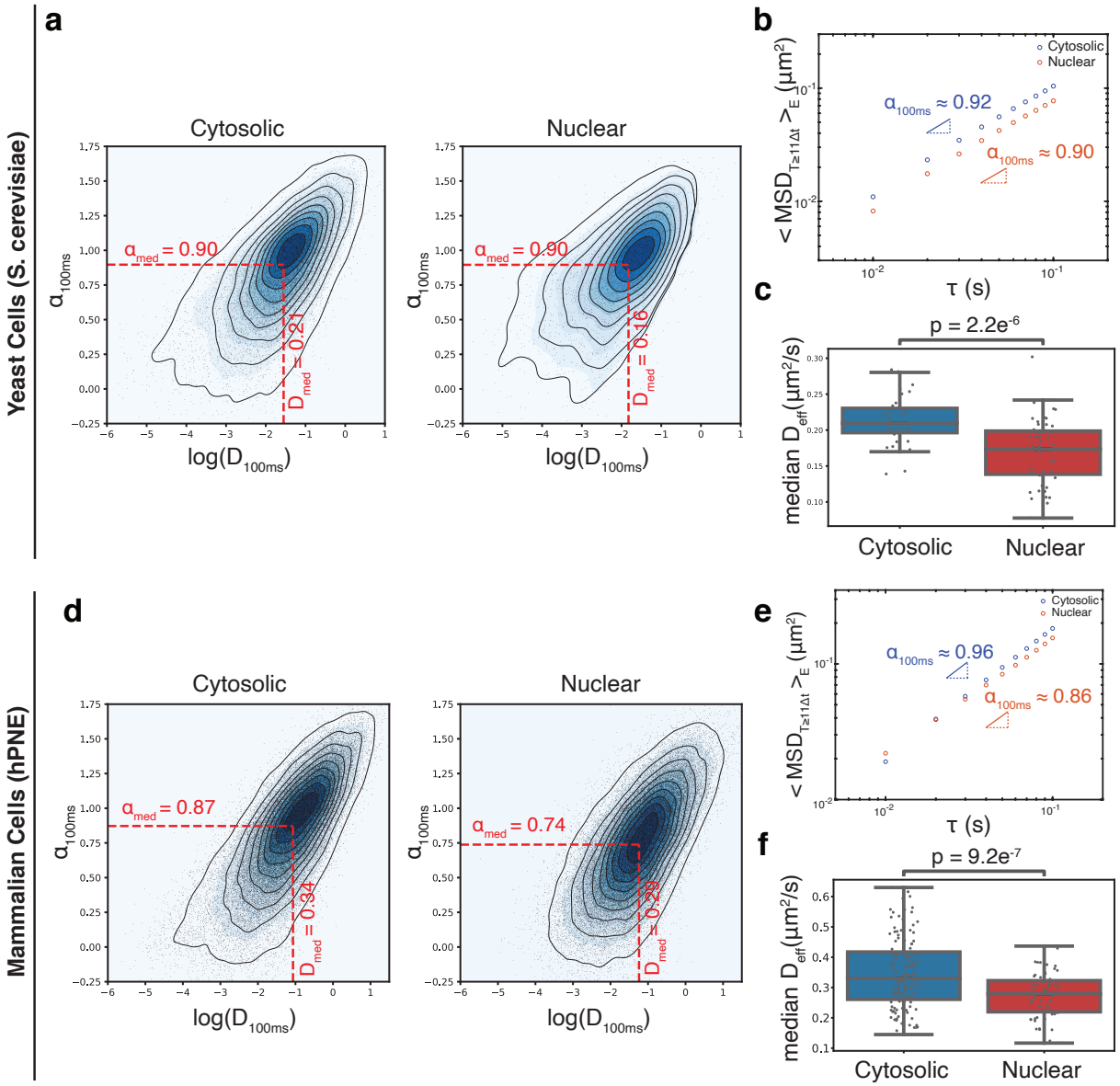

Figure 4: nucGEMs enable comparison of the mesoscale rheology of the nucleus and cytosol. Quantification of nucGEM movement reveals the distinct mesoscale rheological properties of the nucleoplasm and cytosol in both yeast (*S. cerevisiae*, **a-e**), and mammalian cells (hPNE, **f-h**). **a**. Density plot of diffusion coefficient $\log(D_{100ms})$ versus anomalous exponent α_{100ms} for individual GEM trajectories both in cytosol (left) and nucleus (right) of *S. cerevisiae*, with their median values highlighted by red dashed lines. **b**. Ensemble- and time-averaged mean-squared displacement (MSD) versus time delay (τ) with fits to determine α_{100ms} values for nuclear (red) and cytosolic (blue) GEM trajectories in *S. cerevisiae* that have more than 10 time points. In **a-b**, n=10,706 (cytosolic) and n=2969 (nuclear) trajectories. **c**. Box plots of the median effective diffusion coefficients (D_{eff}) of trajectories from single video fields of view of *S. cerevisiae* cells; n=26 (cytosol) and n=51 (nucleus). The horizontal lines in the boxes represent the 25th, 50th, and 75th percentile values with whiskers extending to points that lie within 1.5 times the 25-75th interquartile range. P-values are from a Student's t-test to assess statistical differences between cytosolic and nuclear diffusion. **d**. Density plot of diffusion coefficient $\log(D_{100ms})$ versus anomalous exponent α_{100ms} for individual GEM trajectories both in cytosol (left) and nucleus (right) of human pancreatic (hPNE) cells. **e**. Ensemble- and time-averaged mean-squared displacement (MSD) versus time-step (τ) with fits to determine α_{100ms} values for nuclear (red) and cytosolic (blue) GEM trajectories in hPNE cells with more than 10 time points. In f-g, n=32339 (cytosolic) and n=32971 (nuclear) trajectories. **f**. Box plot of the median effective diffusion coefficients (D_{eff}) of trajectories from individual hPNE cells; n=127 (cytosol) and n=59 (nucleus).

Subdiffusive behavior ($\alpha_{100ms} < 1$) can arise for multiple reasons including interactions with the cell and local or global caging of particles(Meroz and Sokolov 2015). To assess possible origins for the subdiffusive motion of GEMs, we analyzed angle correlations in our data compared to simulated Brownian motion. The angle correlations of GEMs in both the nucleus and cytosol were significantly different from the randomized angles, indicating deviation from Brownian motion (Supplementary Fig. 7b). At time scales greater than 20 ms, angle correlations were negative, consistent with local confinement forcing particles to reverse their direction. Interestingly, angle correlations were positive for very short time-scales, suggesting slightly ballistic behavior, consistent with external non-equilibrium forces imposed by active matter. By combining the time-scale at which the angle correlation of particles within the nucleus and cytosol intercept the origin, i.e. the point at which the mean direction changed from forward to backward, with the effective diffusion of particles D_{eff}, we can estimate the length-scale at which GEMs are confined within each subcellular environment. Through this analysis, we found effective confinement sizes (effective directional displacement) of around 100 nm for GEMs in both the cytosol and nucleus of *S.cerevisiae* (Supplementary Fig. 7c). Therefore, the subdiffusive motion of GEMs may be attributed to confinement within both the cytosol and nucleus. However, these effective confinement sizes are average properties, and are likely to be due to multiple factors including collisions with crowders, and confinement within local polymer meshes; they do not imply the existence of any kind of regular, static structure within the cell.

To investigate the degree of non-specific interactions between GEMs and subcellular structures, we investigated the ergodicity of our data, which is the difference between the effective diffusion D_{eff} obtained from time versus spatially-averaged trajectories. Ergodicity breaking (EB) can be indicative of interactions with the cellular environment or local heterogeneities. This phenomenon can be quantified with an ergodicity breaking parameter, which is zero when there are no interactions and becomes higher with stronger interactions. We found that the D_{eff} from time-averaging has much broader distribution compared to D_{eff} from ensemble-averaging, which revealed breaking of ergodicity in both the nucleus and the cytosol (Supplementary Fig. 7d, 7f, 8d, 9d). The EB parameters were similar in both the nucleus and cytosol (Supplementary Fig. 7e, 7g, 8e, and 9e), which could suggest a similar degree of non-specific interactions of GEMs with other structures in these two compartments.

Together, these results suggest that the mobility of mesoscale (40 nm) GEMs is distinct in the nucleus and cytosol. The motion in both compartments is likely affected by crowding, confinement, and non-specific interactions. Importantly, the motion of mesoscale particles in mammalian cell lines is more rapid in the cytoplasm than the nucleus, but the opposite is true for nanoscale particles(Phair and Misteli 2000). This highlights the importance of investigating the physical properties of cells at multiple length-scales.

Discussion

The mesoscale properties of the cytosol have been probed with well-defined genetically-encoded(Delarue et al. 2018) and non-biological(Etoc et al. 2018) nanoparticles, but there was previously very limited information for the nucleoplasm due to a lack of tools for mesoscale microrheology. Larger 100 nm nanospheres were previously used to discover important viscoelastic properties of the nucleus(Tseng et al. 2004), but we believe that these particles are large enough that they are reporting on chromatin properties rather than the fluid phase of the nucleoplasm. Synthetic(D. S. W. Lee, Wingreen, and Brangwynne 2021) and naturally occurring(Xiang et al. 2021) condensates have provided some of the best insights to date in mammalian cells and bacterial nucleoids respectively, but these probes do not assemble to a defined size and are derived from *Eukaryotic* proteins, leading to strong interactions with the cellular environment, as indicated by strongly subdiffusive behavior. We developed nucGEMs to surmount these limitations: they assemble to a defined size and geometry and are relatively passive, with no specific interactions beyond electrostatic interactions from the charge of the fluorescent protein. Furthermore, nucGEMs are easy to use: no microinjection or laborious sample preparation

is required, allowing the high throughput characterization of many cells in diverse conditions, and enabling the rheological characterization of many species for the first time. For example, it is impossible to use microinjection or micropinocytosis to introduce particles into microorganisms that have cell walls, including powerful genetic systems such as *S. cerevisiae* and *S. pombe*, but we easily introduced nucGEMs into these organisms. Moreover, because nucGEMs move rapidly, a few seconds of imaging generates thousands of traces, to characterize the mesoscale physical properties of the nucleoplasm at high throughput and sub-cellular resolution. Finally, after assembly nucGEMs have precisely the same size and surface properties as our previously reported cytosolics GEMs(Delarue et al. 2018), allowing meaningful comparison of the mesoscale rheological properties of the cytosol and nucleoplasm.

There are limitations in the physical interpretation of microrheology data for both technical and biological reasons. The main current technical limitation is that the data are two dimensional. The ideal imaging rate for nucGEMs is 100 Hz (10 ms frame-rate). This rapid imaging means that experiments are high-throughput, but it is currently difficult to obtain three dimensional data with standard microscope configurations (although engineered point-spread functions are a promising potential solution(Pavani et al. 2009)). Therefore, our imaging was mostly limited to a two-dimensional plane, and as a consequence, track-lengths are often terminated by particles going out of focus. We restrict our analysis to tracks of greater than ten time-steps, but for meaningful comparison between tracks, we also curtail all tracks to this length. There is significant statistical (sampling) noise from these relatively short tracks, which is certain to contribute to the spread of effective diffusion coefficients (D_{eff}) and anomalous exponents presented in Figs. 4a and d.

We caution against over interpretation of the anomalous exponent α. In this study, we explicitly report on this exponent at a single timescale of 100 ms (α_{100ms}). However, different physical phenomena dominate at longer and shorter timescales. For instance, diffusion in a colloidal system is strongly time-dependent: at very short timescales, the effective diffusion coefficient is dictated by the solvent, but on longer timescales, decreases to a steady value set by collisions with crowders. In the transition between these two regimes, there is a mixture of behaviors, with rapid diffusion followed by collisions with crowders that locally and temporarily confine the particle, giving a subdiffusive behavior with an anomalous exponent α of below 1. Additionally, when diffusion occurs in a spatially confined environment, both effective diffusion coefficient and α progressively drop to 0. Thus, two non-mutually exclusive reasons for α values below 1 are local binding, and local or global confinement by steric interactions. It is impossible to design a completely passive particle that does not have some interactions with the cellular environment because of the enormous complexity and diversity of constituents of the cell. The surface properties of GEMs are largely defined by the properties of the densely arrayed fluorescent proteins that face toward the cellular environment. This presents a negatively charged surface that will necessarily undergo electrostatic interactions with positively charged structures in the cell. However, it has been reported that a negative surface charge is far more favorable than a positive charge in this respect(Schavemaker, Śmigiel, and Poolman 2017), perhaps because the most abundant cellular structures (ribosomes in the cytosol, nucleic acids in the nucleus) are negatively charged. Moreover, small net charges of proteins are likely to be negligible compared to solvent friction, and could be modeled by an effective increase in the friction (Makarov and Hofmann 2021). Thus, the most likely explanation for the observed α value below 1 is an effective confinement, which could be due to local crowders or subcellular structuration, as well as the natural physical boundaries of the cell and nucleus.

Finally, there are limitations in the application of simple physical models to interpret cellular microrheology data. The cytosol and nucleoplasm are not homogenous materials, but rather complex, non-equilibrium environments. The cell is highly dynamic, and local rearrangements will constantly modify physical properties invalidating mean field assumptions and potentially contributing to the observed ergodicity breaking. However, the large datasets that we can now generate present exciting possibilities for the development of new theoretical and simulation frameworks to understand the material properties of the cell. Furthermore, we can more effectively investigate the impact that this unusual physical environment might have on molecular biology.

Using nucGEMs, we found that the nucleus is more crowded than the cytosol at the mesoscale, which contrasts with the nanoscale where the converse is true (Phair and Misteli 2000). We find that nucGEMs are excluded from heterochromatin and the nucleolus, supporting the hypothesis that some complexes of similar size (e.g. RNA polymerase, mediator, BAF) may be physically excluded from this dense chromatin. In support of this idea, nucGEMs are ejected from the nucleus of mammalian cells at every mitosis, highlighting the dramatic cellular organization that can be achieved through changes in local material properties. We now have a powerful technology that can investigate the rheological properties of the nucleoplasm in high-throughput, thus enabling discovery of mechanisms that control these properties and the impact of the physical properties of the nucleus on biological processes. The size and surface properties of nucGEMs and cytGEMs are identical, allowing comparison of the physical properties of these compartments. Finally, cytGEMs and nucGEMs can be implemented in multiple organisms across the tree of life, including those with a cell wall, providing insights into the evolution of fundamental physical properties of the cell.

References

Akita, Fusamichi, Khoon Tee Chong, Hideaki Tanaka, Eiki Yamashita, Naoyuki Miyazaki, Yuichiro Nakaishi, Mamoru Suzuki, et al. 2007. “The Crystal Structure of a Virus-like Particle from the Hyperthermophilic Archaeon Pyrococcus Furiosus Provides Insight into the Evolution of Viruses.” *Journal of Molecular Biology* 368 (5): 1469–83.

Boettcher, Barbara, and Yves Barral. 2013. “The Cell Biology of Open and Closed Mitosis.” *Nucleus* 4 (3): 160–65.

Carlini, Lina, Gregory P. Brittingham, Liam J. Holt, and Tarun M. Kapoor. 2020. “Microtubules Enhance Mesoscale Effective Diffusivity in the Crowded Metaphase Cytoplasm.” *Developmental Cell* 54 (5): 574–82.e4.

Crick, FHC, and Hughes, AFW. 1950. “The Physical Properties of Cytoplasm: A Study by Means of the Magnetic Particle Method Part I. Experimental.” *Experimental Cell Research* 1 (1): 37–80.

Cuylen-Haering, Sara, Mina Petrovic, Alberto Hernandez-Armendariz, Maximilian W. G. Schneider, Matthias Samwer, Claudia Blaukopf, Liam J. Holt, and Daniel W. Gerlich. 2020. “Chromosome Clustering by Ki-67 Excludes Cytoplasm during Nuclear Assembly.” *Nature*, September. https://doi.org/10.1038/s41586-020-2672-3.

Delarue, M., G. P. Brittingham, S. Pfeffer, I. V. Surovtsev, S. Pinglay, K. J. Kennedy, M. Schaffer, et al. 2018. “mTORC1 Controls Phase Separation and the Biophysical Properties of the Cytoplasm by Tuning Crowding.” *Cell* 174 (2): 338–49.e20.

Dey, Gautam, Siân Culley, Scott Curran, Uwe Schmidt, Ricardo Henriques, Wanda Kukulski, and Buzz Baum. 2020. “Closed Mitosis Requires Local Disassembly of the Nuclear Envelope.” *Nature* 585 (7823): 119–23.

Ehrig, T., D. J. O’Kane, and F. G. Prendergast. 1995. “Green-Fluorescent Protein Mutants with Altered Fluorescence Excitation Spectra.” *FEBS Letters* 367 (2): 163–66.

Etoc, Fred, Elie Balloul, Chiara Vicario, Davide Normanno, Domenik Liße, Assa Sittner, Jacob Piehler, Maxime Dahan, and Mathieu Coppey. 2018. “Non-Specific Interactions Govern Cytosolic Diffusion of Nanosized Objects in Mammalian Cells.” *Nature Materials*. https://doi.org/10.1038/s41563-018-0120-7.

Fu, X. D., and T. Maniatis. 1990. “Factor Required for Mammalian Spliceosome Assembly Is Localized to Discrete Regions in the Nucleus.” *Nature* 343 (6257): 437–41.

Hameed, Feroz M., Madan Rao, and G. V. Shivashankar. 2012. “Dynamics of Passive and Active Particles in the Cell Nucleus.” *PloS One* 7 (10): e45843.

Harrison, Andrew W., David A. Kenwright, Thomas A. Waigh, Philip G. Woodman, and Victoria J. Allan. 2013. “Modes of Correlated Angular Motion in Live Cells across Three Distinct Time Scales.” *Physical Biology* 10 (3): 036002.

Heun, P., T. Laroche, K. Shimada, P. Furrer, and S. M. Gasser. 2001. “Chromosome Dynamics in the Yeast Interphase Nucleus.” *Science* 294 (5549): 2181–86.

Kim, Kyoohyun, and Jochen Guck. 2020. “The Relative Densities of Cytoplasm and Nuclear Compartments Are Robust against Strong Perturbation.” *Biophysical Journal* 119 (10): 1946–57.

Lee, Daniel S. W., Ned S. Wingreen, and Clifford P. Brangwynne. 2021. “Chromatin Mechanics Dictates Subdiffusion and Coarsening Dynamics of Embedded Condensates.” *Nature Physics* 17 (4): 531–38.

Lee, K. M., C. Nguyen, A. B. Ulrich, P. M. Pour, and M. M. Ouellette. 2003. “Immortalization with Telomerase of the Nestin-Positive Cells of the Human Pancreas.” *Biochemical and Biophysical Research Communications* 301 (4): 1038–44.

Luby-Phelps, Kate. 2013. “The Physical Chemistry of Cytoplasm and Its Influence on Cell Function: An Update.” *Molecular Biology of the Cell* 24 (17): 2593–96.

Luby-Phelps, K., D. L. Taylor, and F. Lanni. 1986. “Probing the Structure of Cytoplasm.” *The Journal of Cell Biology* 102 (6): 2015–22.

Makarov, Dmitrii E., and Hagen Hofmann. 2021. “Does Electric Friction Matter in Living Cells?” *The Journal of Physical Chemistry. B* 125 (23): 6144–53.

Manzo, Carlo, and Maria F. Garcia-Parajo. 2015. “A Review of Progress in Single Particle Tracking: From Methods to Biophysical Insights.” *Reports on Progress in Physics* 78 (12): 124601.

Marshall, W. F., A. Straight, J. F. Marko, J. Swedlow, A. Dernburg, A. Belmont, A. W. Murray, D. A. Agard, and J. W. Sedat. 1997. “Interphase Chromosomes Undergo Constrained Diffusional Motion in Living Cells.” *Current Biology: CB* 7 (12): 930–39.

McLaughlin, Grace A., Erin M. Langdon, John M. Crutchley, Liam J. Holt, Mark Gregory Forest, Jay M. Newby, and Amy S. Gladfelter. 2019. “3D Neural Network-Based Particle Tracking Reveals Spatial Heterogeneity of the Cytosol.” *Cell*, October, 823286.

Meroz, Yasmine, and Igor M. Sokolov. 2015. “A Toolbox for Determining Subdiffusive Mechanisms.” *Physics Reports*. https://doi.org/10.1016/j.physrep.2015.01.002.

Mohr, Dagmar, Steffen Frey, Torsten Fischer, Thomas Güttler, and Dirk Görlich. 2009. “Characterisation of the Passive Permeability Barrier of Nuclear Pore Complexes.” *The EMBO Journal* 28 (17): 2541–53.

Molines, A. T., J. Lemière, C. H. Edrington, C-T Hsu, I. E. Steinmark, K. Suhling, G. Goshima, L. J. Holt, G. J. Brouhard, and F. Chang. 2020. “Physical Properties of the Cytoplasm Modulate the Rates of Microtubule Growth and Shrinkage.” *Cold Spring Harbor Laboratory*. https://doi.org/10.1101/2020.10.27.352716.

Parry, Bradley R., Ivan V. Surovtsev, Matthew T. Cabeen, Corey S. O’Hern, Eric R. Dufresne, and Christine Jacobs-Wagner. 2014. “The Bacterial Cytoplasm Has Glass-like Properties and Is Fluidized by Metabolic Activity.” *Cell* 156 (1-2): 183–94.

Pavani, Sri Rama Prasanna, Michael A. Thompson, Julie S. Biteen, Samuel J. Lord, Na Liu, Robert J. Twieg, Rafael Piestun, and W. E. Moerner. 2009. “Three-Dimensional, Single-Molecule Fluorescence Imaging beyond the Diffraction Limit by Using a Double-Helix Point Spread Function.” *Proceedings of the National Academy of Sciences of the United States of America* 106 (9): 2995–99.

Phair, R. D., and T. Misteli. 2000. “High Mobility of Proteins in the Mammalian Cell Nucleus.” *Nature* 404 (6778): 604–9.

Rivas, Germán, and Allen P. Minton. 2018. “Toward an Understanding of Biochemical Equilibria within Living Cells.” *Biophysical Reviews* 10 (2): 241–53.

Schavemaker, Paul E., Wojciech M. Śmigiel, and Bert Poolman. 2017. “Ribosome Surface Properties May Impose Limits on the Nature of the Cytoplasmic Proteome.” *eLife* 6 (November): 21.

Scherer, W. F., J. T. Syverton, and G. O. Gey. 1953. “Studies on the Propagation in Vitro of Poliomyelitis Viruses. IV. Viral Multiplication in a Stable Strain of Human Malignant Epithelial Cells (strain HeLa) Derived from an Epidermoid Carcinoma of the Cervix.” *The Journal of Experimental Medicine* 97 (5): 695–710.

Stetten, David von, Marjolaine Noirclerc-Savoye, Joachim Goedhart, Theodorus W. J. Gadella Jr, and Antoine Royant. 2012. “Structure of a Fluorescent Protein from Aequorea Victoria Bearing the Obligate-Monomer Mutation A206K.” *Acta Crystallographica. Section F, Structural Biology and Crystallization Communications* 68 (Pt 8): 878–82.

Tokunaga, Makio, Naoko Imamoto, and Kumiko Sakata-Sogawa. 2008. “Highly Inclined Thin Illumination Enables Clear Single-Molecule Imaging in Cells.” *Nature Methods* 5 (2): 159–61.

Tseng, Yiider, Jerry S. H. Lee, Thomas P. Kole, Ingjye Jiang, and Denis Wirtz. 2004. “Micro-Organization and Visco-Elasticity of the Interphase Nucleus Revealed by Particle Nanotracking.” *Journal of Cell Science* 117 (Pt 10): 2159–67.

Vries, Anthony H. B. de, Bea E. Krenn, Roel van Driel, Vinod Subramaniam, and Johannes S. Kanger. 2007. “Direct Observation of Nanomechanical Properties of Chromatin in Living Cells.” *Nano Letters* 7 (5): 1424–27.

Weigel, Aubrey V., Blair Simon, Michael M. Tamkun, and Diego Krapf. 2011. “Ergodic and Nonergodic Processes Coexist in the Plasma Membrane as Observed by Single-Molecule Tracking.” *Proceedings of the National Academy of Sciences of the United States of America* 108 (16): 6438–43.

Weill, Uri, Ido Yofe, Ehud Sass, Bram Stynen, Dan Davidi, Janani Natarajan, Reut Ben-Menachem, et al. 2018. “Genome-Wide SWAp-Tag Yeast Libraries for Proteome Exploration.” *Nature Methods* 15 (8): 617–22.

Xiang, Yingjie, Ivan V. Surovtsev, Yunjie Chang, Sander K. Govers, Bradley R. Parry, Jun Liu, and Christine Jacobs-Wagner. 2021. “Interconnecting Solvent Quality, Transcription, and Chromosome Folding in Escherichia Coli.” *Cell*. https://doi.org/10.1016/j.cell.2021.05.037.

Zapata-Hommer, Otilia, and Oliver Griesbeck. 2003. “Efficiently Folding and Circularly Permuted Variants of the Sapphire Mutant of GFP.” *BMC Biotechnology* 3 (May): 5.

Zhou, Huan-Xiang, Germán Rivas, and Allen P. Minton. 2008. “Macromolecular Crowding and Confinement: Biochemical, Biophysical, and Potential Physiological Consequences.” *Annual Review of Biophysics* 37 (1): 375–97.

Zidovska, Alexandra. 2020. “The Rich Inner Life of the Cell Nucleus: Dynamic Organization, Active Flows, and Emergent Rheology.” *Biophysical Reviews* 12 (5): 1093–1106.

Zidovska, Alexandra, David A. Weitz, and Timothy J. Mitchison. 2013. “Micron-Scale Coherence in Interphase Chromatin Dynamics.” *Proceedings of the National Academy of Sciences* 110 (39): 15555–60.

Methods

Reagent	Source	Identifier
Plasmids		
psPAX2	Addgene	12260
pMD2.G	Addgene	12259
pINO4-SV40NLS-PfV-Sapphire-HO	Holt lab	pLH1459
pPGK1-Cas9-tPGK1-URA3	Tom Ellis lab	pLH1460
gRNA-HO	Holt lab	pLH1461
pRS305-pINO4-PfV-Sapphire	Holt lab	pLH497
pFA6a-link-ymRuby2-SpHIS5	Holt lab	pLH1662
pRS305-pINO4-SV40NLS-PfV-Sapphire	Holt lab	pLH941
pRS305-PINO4-PfV-Sapphire-SV40NLS	Holt lab	pLH637
pUBC-SV40NLS-PfV-Sapphire-IRES-H2B-mCherry	Holt lab	pLH1559
pUBC-PfV-Sapphire-IRES-H2B-mCherry	Holt lab	pLH1876
leu1-32::pREp41X-SV40NLS-PfV-Sapphire	Chang lab	
leu1-32::pREp41X-PfV-Sapphire	Chang lab	
Chemicals and consumables		
VECTASHIELD® Mounting Medium with DAPI	Vector laboratories	H-1800-10
FuGENE® HD Transfection Reagent	Promega	E2312
Ro-3306	MedChemExpress	HY-12529

Plasmid construction: The pLH1559 construct was cloned from a previous mammalian codon optimized plasmid (Delarue et al., 2018). pLH1876 was derived by restriction digestion of pLH1559 to remove the SV40NLS.

Yeast strains:
Culture: Strains were grown in synthetic complete media + 2% dextrose (SCD) according to standard Cold Spring Harbor Protocols at 30^0C in a rotating incubator unless otherwise stated.

Strain	Source	Identifier
S. cerevisiae		
BY4741, ura3Δ0, his3Δ0, leu2Δ0, met15Δ0	Holt lab	LH2145
BY4741, HO::pINO4-SV40NLS-PfV-Sapphire	Holt lab	LH4046
BY4741, leu2Δ::pINO4::pINO4-PfV-Sapphire-LEU2	Holt lab	LH4248
BY4741, HO::pINO4-SV40NLS-PfV-Sapphire, Nup49-ymRuby2::SpHIS5	Holt lab	LH4278
BY4741, leu2Δ::pINO4-PfV-Sapphire-SV40NLS::LEU2	Holt lab	LH2859
BY4741, leu2Δ::pINO4-SV40NLS-PfV-Sapphire::LEU2	Holt lab	LH3080
BY4741, NOP4::pTEF2-mCherry-Nop4::NatR, his3Δ1, leu2Δ0, met15Δ0, ura3Δ0, lys+, can1Δ::GAL1pr-SceI::STE2pr-SpHIS5, lyp1Δ::STE3pr-LEU2	SWAT library(Weill et al. 2018)	LH4152
BY4741, NOP4::pTEF2-mCherry-Nop4::NatR, HO::pINO4-SV40NLS-PfV-Sapphire, can1Δ::GAL1pr-SceI::STE2pr-SpHIS5, lyp1Δ::STE3pr-LEU2	Holt lab	LH4162
S. pombe		
h+, ish1-mCherry:hphMX6, leu1-32::pREp41X-SV40NLS-PfV-Sapphire, ade6-M216, ura4-D18, his3-D1	Chang lab	

Transformation: *S. cerevisiae* transformation was according to standard Cold Spring Harbor Protocols.

Mammalian cell culture and treatments:
HeLa and HEK293T cells were a kind gift from Prof. Jef Boeke (Institute for Systems Genetics, NYU Langone), hTERT-immortalized HPNE cells were a kind gift from Prof. Diane Simeone (NYU Langone), and mouse neural progenitor cells (NPCs) isolated from E14.5 embryos were a kind gift of Dr. Mario Pende (INEM Paris, France). HeLa and HEK293T cells were grown in DMEM (Gibco, Cat. No. 11995073) supplemented with 10%FBS (Gemini bio-products, Cat. no. 100-106), 2mM L-Glutamine (Gibco, Cat. No. 25030-081) and Penstrep (Gibco, Cat. No.15140-122). hPNE cells were grown in RPMI 1640 (Gibco, Cat. No.11875085) supplemented with 10% FBS (Gemini bio-products, Cat. no. 100-106) and Penstrap (Gibco, Cat. No.15140-122). NPCs were grown using the NeuroCult TM Proliferation kit (Stem Cell California Inc., Cat. No. 05702) and media supplemented with 20ng/ml of human recombinant epithelial growth factor (EGF - STEMCELL Technologies, Cat. No. 78006). All cells were grown in a humidified incubator atmosphere at 37°C and 5% CO_2. NPCs were differentiated by culturing in the absence of EGF in N2/B27 media (Neurobasal-A medium -Thermo Scientific, Cat. No. 10888022) supplemented with N2/B27 with Vitamin A (Thermo Scientific, Cat. No. 17502-048/17504044) and 0.4 mM ascorbic acid (Sigma-Aldrich, Cat. No. A8960) for at least 6 days before fixation.

Lentivirus production and cell transduction:
HEK293T cells ($9x10^6$ per 15 cm dish) were plated in antibiotic free DMEM (Gibco, Cat. No. 11995073) supplemented with 10%FBS (Gemini bio-products, Cat. no. 100-106), 2mM L-Glutamine (Gibco, Cat. No. 25030-081). The next day, cells were transfected with transgene plasmid together with lentivirus packaging plasmids psPAX2 (Addgene, Cat. No. 12260) and pMD2.G (AddGene, Cat. No. 12259), using fuGENE HD™ transfection reagent following manufacturer's protocol. 24 hours later, antibiotic free DMEM was replaced and supernatants collected at 48 and 72 h post-transfection and stored at 4^0C. Virus titers were concentrated by centrifugation at 4,000 rcf for 40 minutes in an Amicon Ultra-15 30 KDa centrifugal filter (MilliporeSigma, Cat. No. UFC903024). Concentrated viral suspensions were aliquoted and stored at -80^0C until later use. Lentivirus was introduced into cell lines of interest via reverse transduction with 1-10 µL of concentrated virus in fresh media, and replacing media after 24 hours. After cell lines stabilized, they were frozen in 10% DMSO (Sigma-Aldrich, Cat. no. D2650-100) in FBS (Gemini bio-products, Cat. no. 100-106) and thawed for use in experiments as needed.

Cell cycle synchronization and imaging:
200,000 HPNE cells stably expressing nucGEMs were plated in 6-well glass bottom dishes. 10uM CDK1 inhibitor Ro-3306 (MedChem Express, Cat. No. HY-12529) was added to each well and was incubated overnight (16-20 hours). On the day of the experiment, cells were mounted on a Nikon spinning disk confocal scanning microscope, equipped with a 63x/1.4 numerical aperture (NA) objective and incubator to maintain 37°C and 5% CO_2. Cells were manually selected for imaging and imaged once in G_2 before synchronized release. To release cells into mitosis, cells were washed 3 times with pre-warmed PBS then supplied with fresh media without the drug. Time-lapse acquisition was performed with time intervals of 15 mins for 3-5 hours. Cells Undergoing mitosis were further processed and analysed using Fiji/imageJ (version 2.3.0). Images from a single focal plane were cropped and processed (subtract background, gaussian blur and adjust threshold) to generate representative images. Fluorescence intensities within the nucleus and cytoplasm were measured by segmenting nuclear area with SiRDNA fluorescence or hand-sampling within the cytoplasm and reported using mean gray values in the 488 nm channel. Values were averaged and plotted with standard deviation in Microsoft Excel (version 16.54).

Immunofluorescence analysis:
Cells were fixed with 4% formaldehyde (15 min), permeabilized with 0.2% Triton X-100 in phosphate-buffered saline (PBS) for 15 min, blocked with 1% bovine serum albumin in PBS (blocking buffer) for 1 h, incubated with primary antibodies (diluted in blocking buffer) for overnight in humidified chamber at 4^0C. The next day, cells were washed three times with PBS (10min interval) and then incubated in secondary antibodies (1: 400 in blocking solution) for 1 h in the dark at RT, followed by three PBS washes. Samples were mounted with VectaShield mounting medium containing 4′,6-diamidino-2-phenylindole (DAPI). Cells were incubated with SiR-DNA for 1 h prior to fixation, in cases where SiR-DNA was used as a DNA marker. Image acquisition was performed using Nikon spinning disk confocal scanning microscope, equipped with a 63X/1.4 numerical aperture (NA) objective. Images were processed using FIJI/ImageJ2 (version 2.3.0). All images unless mentioned otherwise are single optical sections of the images (step size 0.5µm). PearsonR method: Pearson correlation coefficients were calculated by comparing pixel intensities of each channel.

Subcellular compartment	Marker	Source and catalog No.	Dilution
Heterochromatin	Histone H3 (tri methyl K9)	Abcam (ab8898)	1:500
Nuclear Speckle	SC-35 Nuclear Speckle Marker	Abcam (ab11826)	1:250
Nucleolus	NPM1 (Nucleophosmin)	Abcam (ab10530)	1:500
Euchromatin	Histone H3 (acetyl K27)	Abcam (ab4729)	1:500
Nuclear envelope	Lamin B1	Abcam (ab16048)	1:500
Neural soma and dendrites	MAP2	Proteintech (17490-1-AP)	1:500
DNA	SiR-DNA	Cytoskeleton (CY-SC007)	1:5000
Secondary Antibodies	Goat Anti-Rabbit IgG (H+L)-Alexa 568	Invitrogen (A11036)	1:1000
	Goat Anti-Mouse IgG (H+L)-Alexa 594	Invitrogen (A11032)	1:1000

Cell Growth and Viability Assay:
For cell growth analysis, 20,000 cells were seeded in a 24-well plate. After 24hrs cells were trypsinized using TrypLE™ Express Enzyme (GIBCO, Cat. no. 12604039) and total number of live cells were counted based on Trypan Blue stain using Countess® II FL Automated Cell Counter (Invitrogen, Cat. No. AMQAF2000). Metabolic activity was assayed as a measure of cell viability using PrestoBlue™ (Invitrogen, Cat. no. A13261). 20,000 cells were seeded per well in a 24-well plate and PrestoBlue™ was added by 1/10th volume of the media in the well 24 hours later. After 1 hr incubation, the supernatant was transferred to a 96-well flat bottom plate and fluorescence was measured at excitation wavelength of 560 nm and emission at 590 nm using a microplate reader.

HILO Imaging of GEMs:
GEM particles in yeast cells were imaged using a TIRF Nikon TI Eclipse microscope in partial TIRF mode at 488 nm excitation with 100% power. The emitted fluorescent signals were transmitted through a 100x objective (100x DIC, Nikon, oil NA = 1.45, part number = MRD01905; 100x Phase, Nikon, oil NA = 1.4, part number = MRD31901) and recorded with a sCMOS camera (Zyla, Andor, part number = ZYLA-4.2p-CL10). GFP filter set (ET-EGFP (FITC/Cy2), Chroma, part number = 49002) was embedded within the light path, which includes an excitation

filter (Excitation wavelength/ Bandwidth (FWHM) = 470/40 nm), a dichroic mirror (long pass beamsplitter, reflecting < 495 nm and transmitting > 495 nm wavelength) and an emission filter (Emission wavelength/ Bandwidth (FWHM) = 525/50 nm). Each GEM movie was composed of images acquired every 10 ms for a total 4 s.

Confocal Imaging of GEMs:
Micrographs were acquired on a Nikon Eclipse Ti Eclipse microscope mounted with Yokogawa CSU-X1 spinning disk unit, NIDAQ AOTF multilaser unit, and Prime 95B camera operating on Nikon NIS-Elements AR (v 5.21.03) software. We used CFI Apo 60x/N.A-1.49/.12 TIRF objective with a 470/40m excitation filter and ET525/36m emission filter (Chroma Technology Corp) in all mammalian acquisitions. Using a 488 nm laser the sapphire fluorophore was excited using 100% power and images were collected from a single focal plane at 100fps, binning 1, 512X512, and 8-bit pixel depth for 2 to 4 seconds.

Quantification of mesoscale rheology:

Time-averaged, ensemble-time-averaged mean-square displacement (MSD):
For every 2D trajectory, we calculated the time-averaged mean-square displacement (MSD) at different time intervals:

$$< \Delta r^2(\tau) >_T = < [x(t+\tau) - x(t)]^2 + [y(t+\tau) - y(t)]^2 >_T \quad (1)$$

where '$<>_T$' represents time averaging for each trajectory of all displacements under time interval τ.

To reduce tracking error due to particles moving in and out of the focal plane, we selected particle trajectories with more than 10 time points. We then fitted the time-averaged MSD of each selected trajectory with power-law time dependence based on the first 10 time intervals (100ms). Density map of α vs. D_{100ms} can then be plotted for all trajectories (Etoc et al. 2018) (Fig. 4a, 4f and S5a, S6a).

$$MSD(\tau)_T = 4D_{100ms}\tau^{\alpha} \quad (2)$$

where α indicates diffusion property, with $\alpha = 1$ being Brownian motion, $\alpha < 1$ suggests sub-diffusive motion and $\alpha > 1$ as super-diffusive motion. D_{100ms} is the diffusion coefficient with the unit of $\mu m^2/s^{\alpha}$.

For better comparison of GEM diffusivity under different conditions, we also used the effective diffusion coefficient for characterization due to the unifying of its unit as $\mu m^2/s$. Time-averaged MSD for each trajectory is fitted using a linear time dependence at first 10 time intervals:

$$MSD(\tau)_T = 4D_{eff}\tau \quad (3)$$

where D_{eff} is the effective diffusion coefficient for each trajectory.
We then used median value of D_{eff} among all trajectories within either each field of view for yeast cells (512x512 pixels including several yeast cells) or each individual mammalian cell and plotted as each individual dot on bar graphs for characterizing GEM mobility in different conditions (Fig. 4c, 4h, S5c and S6c).

Ensemble-time averaged MSD was also applied for better indication of α at each condition and was subsequently fitted with the power-law time dependence at first 10 time intervals.

$$MSD(\tau)_{T-ens} = << \Delta r^2(\tau) >_T >_{ens} \quad (4)$$

$$MSD(\tau)_{T-ens} = 4D\tau^{\alpha} \quad (5)$$

where ensemble-time averaged MSD is the ensemble-averaging among all time-averaged MSD for trajectories that are above a certain trajectory length cutoff (10 time points for most figures: Fig. 4b, 4g, S5b and S6b; 20, 50, 100 for Fig. S4a).

Ensemble-averaged MSD and breaking of ergodicity:

At every time point, we calculated the ensemble-averaged mean-square displacement (MSD) for all trajectories based on:

$$< \Delta r^2(\tau, t) >_{ens} = < [x(t+\tau) - x(t)]^2 + [y(t+\tau) - y(t)]^2 >_{ens} \quad (6)$$

where '$<>_{ens}$' represents ensemble averaging for all selected trajectories with displacements under time interval τ at time point t.

For simplicity, we choose specific time interval $\tau = 20ms$ and directly calculate effective diffusion coefficient without fitting as D_{20ms} using either time-averaged or ensemble-averaged MSD at 20ms time interval (Etoc et al. 2018)(Weigel et al. 2011) (Fig. S4b, S4d, S5d and S6d).

$$D_{20ms-T} = \frac{<\Delta r^2(20ms)>_T}{4*20ms} \quad (7)$$

$$D_{20ms-ens} = \frac{<\Delta r^2(20ms)>_{ens}}{4*20ms} \quad (8)$$

Differences in distribution of time-averaged and ensemble-averaged D_{20ms} suggests ergodicity breaking. To quantify the level of nonergodicity, we calculated ergodicity breaking parameter (EB) based on (Manzo and Garcia-Parajo 2015) (Meroz and Sokolov 2015) (Fig. S4c, S4e, S5e and S6e):

$$EB(\tau) = \frac{Var(<\Delta r^2(\tau)>_T)}{<<\Delta r^2(\tau)>_T>^2} \quad (9)$$

where EB value is dimensionless quantity with its numerator as the variance and its denominator as the square of mean of time-averaged MSD for all selected trajectories at time interval τ.

Angle correlation function and estimate of effective confinement size:

Angle correlation function was calculated for detailed analysis of GEMs movement. For each trajectory, we calculated cosine of angle between displacements under time interval τ. Angle correlation function was then calculated by combining and averaging all $cos(\theta(\tau))$ values within each trajectory as well as among all trajectories.

$$< cos(\theta(\tau)) > = < \frac{\overrightarrow{r(t+\tau)} \cdot \overrightarrow{r(t)}}{|\overrightarrow{r(t+\tau)}||\overrightarrow{r(t)}|} > \quad (10)$$

where $< cos(\theta(\tau)) > = 0$ suggests no angular correlation as Brownian motion, $< cos(\theta(\tau)) > < 0$ suggests anti-persistent angular correlation and $< cos(\theta(\tau)) > > 0$ indicates persistent angular correlation (Harrison et al. 2013) (Fig. 4d).

We could then calculate the characteristic time t_{cross} as the time point when $< cos(\theta(\tau)) >$ changes from positive to negative values. t_{cross} indicated the time scale for directional GEM movements. Combining previously acquired D_{eff} for every condition, we could estimate the effective confinement size for GEM particles in both cytosol and nucleus (Fig. 4e).

$$effective\ confinement\ size = \sqrt{4D_{eff} \cdot t_{cross}} \quad (11)$$

$$std(confinement\ size) = std(D_{eff}) \cdot \sqrt{t_{cross}/D_{eff}} \quad (12)$$

where 'std' represents the standard deviation of variables.

Plasmid, strain and cell line availability

All plasmids will be deposited in Addgene. Yeast strains and human cell lines will be made available upon request.

Data availability

Github: https://github.com/Shutong20/Holtlab-nucGEM-paper-data-repository

Code availability

Matlab codes: https://github.com/Shutong20/Holt-Lab-GEM-analysis
Python code: https://github.com/liamholtlab/GEMspa/releases/tag/v0.11-beta

Acknowledgements

We thank Diane Simeone for the gift of human pancreatic nestin expressing (hPNE) cells, Jef Boeke for HeLa and HEK293 cells, and Mario Pende for Neural Progenitor Cells (NPCs). We thank all members of the Holt lab for assistance and feedback.

Ethics declarations

The authors declare no competing financial interests.